

The kaobook class

**Use this document as a template**

# **Millikelvin Confocal Microscopy of Semiconductor Membranes and Filter Functions for Unital Quantum Operations**

**Customise this page according to your needs**

Tobias Hangleiter\*

July 28, 2025

\* A  $\text{\LaTeX}$  lover/hater

The harmony of the world is made manifest in Form and Number, and the heart and soul and all the poetry of Natural Philosophy are embodied in the concept of mathematical beauty.

– D'Arcy Wentworth Thompson

# Contents

<b>Contents</b>	<b>iii</b>
<b>I A FLEXIBLE PYTHON TOOL FOR FOURIER-TRANSFORM NOISE SPECTROSCOPY</b>	<b>1</b>
<b>1 Introduction</b>	<b>2</b>
<b>2 Theory of spectral noise estimation</b>	<b>4</b>
2.1 Spectrum estimation from time series . . . . .	5
2.2 Window functions . . . . .	7
2.3 Welch's method . . . . .	8
2.4 Parameters & Properties of the PSD . . . . .	9
<b>3 The python_spectrometer software package</b>	<b>11</b>
3.1 Package design and implementation . . . . .	11
3.1.1 Data acquisition . . . . .	11
3.1.2 Data processing . . . . .	13
3.2 Feature overview . . . . .	14
3.2.1 Serial spectrum acquisition . . . . .	15
3.2.2 Live spectrum acquisition . . . . .	18
<b>4 Conclusion and outlook</b>	<b>20</b>
<b>II CHARACTERIZATION AND IMPROVEMENTS OF A MILLIKELVIN CONFOCAL MICROSCOPE</b>	<b>23</b>
<b>1 Introduction</b>	<b>3</b>
<b>2 Characterization of the cryostat performance</b>	<b>4</b>
2.1 Cooling power . . . . .	4
2.2 Electron temperature . . . . .	6
<b>3 Optical path</b>	<b>10</b>
3.1 Light coupling . . . . .	10
3.1.1 Choosing lenses . . . . .	10
3.1.2 Collection efficiency . . . . .	13
3.1.3 Imaging the laser spot . . . . .	16
3.1.4 Cross-polarization extinction . . . . .	17
3.2 Exemplary measurement of non-classical light . . . . .	17
<b>4 Vibration noise</b>	<b>19</b>
4.1 Vibration isolation . . . . .	20
4.1.1 Damping theory . . . . .	20
4.1.2 Microscope isolation concept . . . . .	21
4.2 Accelerometric vibration spectroscopy . . . . .	21
4.3 Optical vibration spectroscopy . . . . .	23
4.3.1 Noise floor . . . . .	26
4.4 Routes for improvement . . . . .	28
<b>5 Conclusion &amp; outlook</b>	<b>30</b>

<b>III OPTICAL MEASUREMENTS OF ELECTROSTATIC EXCITON TRAPS IN SEMICONDUCTOR MEMBRANES</b>	<b>31</b>
<b>6 Introduction</b>	<b>32</b>
<b>7 Photoluminescence and excitons in semiconductors</b>	<b>33</b>
7.1 Photoluminescence in doped GaAs/Al <sub>x</sub> Ga <sub>1-x</sub> As heterostructures . . . . .	34
7.2 The quantum-confined Stark effect . . . . .	35
7.2.1 In-plane confinement . . . . .	37
7.3 Excitonic complexes . . . . .	39
<b>8 The mjolnir measurement framework</b>	<b>40</b>
<b>9 Observations</b>	<b>41</b>
9.1 Transfer-matrix method simulations of the membrane structure . . . . .	41
<b>10 Conclusion &amp; outlook</b>	<b>50</b>
<b>IV A FILTER-FUNCTION FORMALISM FOR UNITAL QUANTUM OPERATIONS</b>	<b>51</b>
<b>APPENDIX</b>	<b>52</b>
<b>A Optical coupling</b>	<b>34</b>
A.1 Collection efficiency . . . . .	34
A.2 Mode profile . . . . .	35
A.3 Fraunhofer diffraction . . . . .	36
<b>B Vibration spectroscopy</b>	<b>38</b>
B.1 Knife-edge measurement . . . . .	38
B.2 Additional vibration spectroscopy data . . . . .	38
<b>C Additional TMM simulations</b>	<b>39</b>
C.1 Dependence on epoxy thickness . . . . .	39
C.2 Optimization of the barrier thickness . . . . .	39
<b>Bibliography</b>	<b>40</b>
<b>List of Terms</b>	<b>42</b>
<b>Declaration of Authorship</b>	<b>43</b>

# List of Figures

2.1	Generated by <code>img/tikz/spectrometer/lockin_dut.tex</code> . . . . .	4
2.2	Generated by <code>img/py/spectrometer/lorentz.py</code> . . . . .	6
2.3	Generated by <code>img/py/spectrometer/pyspeck.py</code> . . . . .	8
2.4	Generated by <code>img/py/spectrometer/pyspeck.py</code> . . . . .	8
2.5	Generated by <code>img/py/spectrometer/pyspeck.py</code> . . . . .	9
2.6	Generated by <code>img/tikz/spectrometer/daq_settings.tex</code> . . . . .	10
3.1	Generated by <code>img/tikz/spectrometer/speck_tree.tex</code> . . . . .	11
3.2	Generated by <code>img/py/spectrometer/pyspeck_workflow.py</code> . . . . .	15
3.3	Generated by <code>img/py/spectrometer/pyspeck_workflow.py</code> . . . . .	16
3.4	Generated by <code>img/py/spectrometer/pyspeck_workflow.py</code> . . . . .	17
3.5	Generated by <code>img/py/spectrometer/pyspeck_workflow.py</code> . . . . .	17
3.6	Generated by <code>img/py/spectrometer/pyspeck_workflow.py</code> . . . . .	17
3.7	Generated by <code>img/py/spectrometer/pyspeck_workflow.py</code> . . . . .	18
3.8	Generated by <code>img/py/spectrometer/pyspeck_live_view.py</code> . . . . .	19
2.1	Generated by <code>img/py/setup/cooling_power.py</code> . . . . .	5
2.2	Generated by <code>img/py/setup/cooling_power.py</code> . . . . .	6
2.3	Generated by <code>img/py/setup/cooling_power.py</code> . . . . .	6
2.4	Generated by <code>img/py/setup/transport.py</code> . . . . .	7
2.5	Generated by <code>img/py/setup/transport.py</code> . . . . .	8
2.6	Generated by <code>img/py/setup/transport.py</code> . . . . .	9
3.1	Generated by <code>img/tikz/setup/optical_path.tex</code> . . . . .	10
3.2	Generated by <code>img/py/setup/single_mode_fiber_coupling.py</code> . . . . .	13
3.3	Generated by <code>img/tikz/setup/emission.tex</code> . . . . .	14
3.4	Generated by <code>img/py/setup/extraction.py</code> . . . . .	15
3.5	Generated by <code>img/py/setup/extraction.py</code> . . . . .	16
3.6	Generated by <code>img/py/setup/imaging.py</code> . . . . .	17
3.7	Generated by <code>img/py/setup/g2.py</code> . . . . .	18
3.8	Generated by <code>img/py/setup/g2.py</code> . . . . .	18
4.1	Generated by <code>img/pdf/setup/springs.py</code> . . . . .	20
4.2	Generated by <code>img/py/setup/vibration_spectroscopy.py</code> . . . . .	23
4.3	Generated by <code>img/tikz/setup/knife_edge.tex</code> . . . . .	23
4.4	Generated by <code>img/py/setup/vibration_spectroscopy.py</code> . . . . .	24
4.5	Generated by <code>img/py/setup/vibration_spectroscopy.py</code> . . . . .	24
4.6	Generated by <code>img/py/setup/vibration_spectroscopy.py</code> . . . . .	25
4.7	Generated by <code>img/py/setup/vibration_spectroscopy.py</code> . . . . .	26
4.8	Generated by <code>img/pdf/setup/vibration_spectroscopy.py</code> . . . . .	28
5.1	Generated by <code>img/py/setup/vibration_spectroscopy.py</code> . . . . .	30
7.1	Generated by <code>img/py/experiment/pl.py</code> . . . . .	34
7.2	Generated by <code>img/py/experiment/qcse.py</code> . . . . .	35
7.3	Generated by <code>img/py/experiment/qcse.py</code> . . . . .	36
7.4	Generated by <code>img/py/experiment/qcse.py</code> . . . . .	37
7.5	Generated by <code>img/py/experiment/qcse.py</code> . . . . .	38
8.1	Generated by <code>img/tikz/experiment/mjolnir_tree.tex</code> . . . . .	40

9.1	Generated by img/py/experiment/tmm.py. . . . .	43
9.2	Generated by img/py/experiment/tmm.py. . . . .	43
9.3	Generated by img/py/experiment/tmm.py. . . . .	44
9.4	Generated by img/py/experiment/tmm.py. . . . .	44
9.5	Sample: Doped M1_05_49-2. $\lambda_{\text{exc}} = 795 \text{ nm}$ . $P = 0.92 \mu\text{W}$	
	Generated by img/py/experiment/pl.py. . . . .	45
9.6	Sample: Honey H13. $\lambda_{\text{exc}} = 795 \text{ nm}$ , $P = 1 \mu\text{W}$ .	
	Generated by img/py/experiment/pl.py. . . . .	46
9.7	Sample: Fig F10. $\lambda_{\text{exc}} = 795 \text{ nm}$ .	
	Generated by img/py/experiment/pl.py. . . . .	46
9.8	Sample: Doped M1_05_49-2. $V_{\text{CM}} = -1.3 \text{ V}$ , $\lambda_{\text{exc}} = 795 \text{ nm}$ . $P = 10 \mu\text{W}$ .	
	Generated by img/py/experiment/pl.py. . . . .	46
9.9	Sample: Doped M1_05_49-2. $V_{\text{CM}} = -1.3 \text{ V}$ , $P = 1 \mu\text{W}$ .	
	Generated by img/py/experiment/pl.py. . . . .	46
9.10	Sample: Doped M1_05_49-2. $V_{\text{CM}} = -1.3 \text{ V}$ , $P = 1 \mu\text{W}$ .	
	Generated by img/py/experiment/pl.py. . . . .	46
9.11	Sample: Doped M1_05_49-2. $V_{\text{CM}} = -1.3 \text{ V}$ , $P = 1 \mu\text{W}$ .	
	Generated by img/py/experiment/pl.py. . . . .	47
9.12	Sample: Doped M1_05_49-2. $V_{\text{CM}} = -1.3 \text{ V}$ , $P = 1 \mu\text{W}$ .	
	Generated by img/py/experiment/pl.py. . . . .	47
9.13	Sample: Doped M1_05_49-2. $V_{\text{CM}} = -1.3 \text{ V}$ , $P = 1 \mu\text{W}$ .	
	Generated by img/py/experiment/pl.py. . . . .	48
9.14	Sample: Doped M1_05_49-2. $V_{\text{DM}} = -2.7 \text{ V}$ , $V_{\text{CM}} = -1.3 \text{ V}$ , $\lambda_{\text{exc}} = 795 \text{ nm}$ .	
	Generated by img/py/experiment/pl.py. . . . .	49
9.15	Sample: Doped M1_05_49-2. $V_{\text{B}} = 0 \text{ V}$ .	
	Generated by img/py/experiment/pl.py. . . . .	49
B.1	. . . . .	38
C.1	Generated by img/py/experiment/tmm.py. . . . .	39
C.2	Generated by img/py/experiment/tmm.py. . . . .	39

**Part I**

**A FLEXIBLE PYTHON TOOL FOR  
FOURIER-TRANSFORM NOISE  
SPECTROSCOPY**

## **Part II**

# **CHARACTERIZATION AND IMPROVEMENTS OF A MILLIKELVIN CONFOCAL MICROSCOPE**



**Part III**

**OPTICAL MEASUREMENTS OF  
ELECTROSTATIC EXCITON TRAPS IN  
SEMICONDUCTOR MEMBRANES**

# Introduction

6



# Photoluminescence and excitons in semiconductors

7

R

ATS The effective masses of the holes along the growth-direction are

$$m_{\text{hh},z}^* = \frac{1}{\gamma_1 - 2\gamma_2} = 0.38 \quad (7.1)$$

$$m_{\text{lh},z}^* = \frac{1}{\gamma_1 + 2\gamma_2} = 0.09 \quad (7.2)$$

with

$$\gamma_1 = 6.8 \quad (7.3)$$

$$\gamma_2 = 2.1. \quad (7.4)$$

In-plane, the masses then become

$$m_{\text{hh},\parallel}^* = \frac{1}{\gamma_1 + \gamma_2} = 0.11 \quad (7.5)$$

$$m_{\text{lh},\parallel}^* = \frac{1}{\gamma_1 - \gamma_2} = 0.21 \quad (7.6)$$

## 7.1 Photoluminescence in doped GaAs/Al<sub>x</sub>Ga<sub>1-x</sub>As heterostructures

The development of remote-doping techniques enabled the growth of extremely high-mobility two-dimensional electron gases (2DEGs) in GaAs/Al<sub>x</sub>Ga<sub>1-x</sub>As heterostructures [1]. In these structures, dopants introduced into the AlGaAs barrier layer some 50 nm away from the GaAs layer and thus spatially separated by a AlGaAs spacer layer. This reduces Coulomb scattering in the 2DEG induced by the doping and produces very high-quality samples as evidenced for example by the observation of the fractional quantum Hall effect [2]. It is hence not at all surprising that early quantum dot experiments also took place in this well-understood material system. While undoped approaches to electron and hole spin qubits in GaAs exist [3–6], they introduce added complications because of the need to electrostatically induce a 2DEG and reliably contacting it [7]. What is more, these issues are exacerbated when the structures need to be thinned down to a membrane [8, 9]. Therefore, to accommodate gate-defined quantum dots (GDQDs) next to the optically active quantum dot (OAQD) in the membrane, the devices measured in this part of the present thesis are fabricated on doped heterostructures hosting a 2DEG. In the following, I discuss the optical behavior of these structures under illumination.<sup>1</sup>

Consider an intrinsic, direct-gap, Zinc-blende semiconductor such as GaAs with a band gap of  $E_g = 1.519$  eV at zero temperature. At the  $\Gamma$ -point, the conduction band is well approximated by a parabolic band with effective mass  $m_c^*/m_e = 0.067$  and is offset by  $E_g/2$  above the Fermi level  $\mu$ . Offset by the same absolute amount in the opposite direction is the valence band, which close to  $\Gamma$  is fourfold degenerate with heavy and light holes with effective masses  $m_{hh}^*/m_e = 0.34$  and  $m_{lh}^*/m_e = 0.09$ , respectively [15]. The third valence band<sup>2</sup> is split off by the spin-orbit interaction and lies 0.34 eV below the other valence bands [16]. Introducing confinement in one direction, for example by doping a GaAs/Al<sub>x</sub>Ga<sub>1-x</sub>As heterojunction or growing a GaAs quantum well (QW) sandwiched between two layers of AlGaAs, lifts the fourfold degeneracy of light and heavy holes and leaves – under usual conditions – the latter as the valence band ground state.

Doping in sufficiently high concentration then raises the Fermi level from mid-gap to inside the conduction band in the plane of confinement, resulting in a band structure as sketched in Figure 7.1. The bands remain parabolic as function of the in-plane wave vector  $k_{||}$  close to  $\Gamma$ . The valence band is filled up to  $\mu$  where, measured from the conduction band edge,  $E_c(k_{||} = k_F) = E_F = \hbar^2 k_F^2 / 2m_c^*$  with the Fermi wave vector  $k_F \sim 10^8 \text{ m}^{-1}$ . Now, absorption of a photon incident on the semiconductor demands conservation of energy and momentum. The latter condition implies that hole and electron have close to equal momentum because  $k_\gamma = 2\pi/\lambda \approx 8 \times 10^6 \text{ m}^{-1}$  is much smaller than  $k_F$ . Thus, excitation of an electron-hole pair from the valence into the conduction band occurs only for  $k \geq k_F$ . By contrast, recombination can take place for any  $k$  in principle. In practice, however, photo-electrons quickly relax down to the Fermi level, and recombination takes place between electrons inside the Fermi sea and photo-holes somewhere in the valence band at  $k \leq k_F$ .<sup>3</sup> The former condition then implies  $E_\gamma \geq E_g + E_F (1 + m_c^*/m_{hh}^*)$  because no free electron states are available in the conduction band below  $\mu$  due to the Pauli exclusion principle and where the term in parentheses is due to the valence band dispersion.

1: The *electrical* behavior is another matter; there, illumination can lead to the creation, trapping, and de-trapping of free charge carriers that alter the transport properties of the device, leading to electrical hysteresis and instability [9–13].

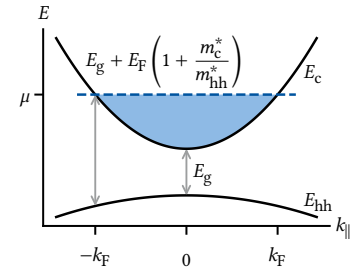


**Figure 7.1:** Band structure diagram of a doped heterostructure (after Reference 14). Due to the *n*-type doping, the conduction band is filled up to the Fermi level  $\mu$ . Photonic excitation of an electron-hole pair can only occur at  $|k| > k_F$  into the free states above  $\mu$  due to the small photon momentum. Recombination can occur within a bandwidth of  $E_F(1 + m_c^*/m_{hh}^*)$ .

2: The valence bands are *p*-like and hence contain contributions from three twofold degenerate atomic orbitals.

3: For sufficiently localized states in real space, a wide range of  $k$  states in the valence band is available for recombination as states are extended in  $k$ -space. We can estimate the localization length required for states up to  $k_F$  to participate by  $\Delta x \geq 1/2\Delta k = 1/2k_F \sim 5 \text{ nm}$  for a typical 2DEG.

Free electron-hole pairs created by photo-excitation can form hydrogenic bound states due to the Coulomb attraction of their opposite electric charges, *excitons*. In two dimensions, this effect is strongly enhanced due to the increased overlap of electron and hole wavefunctions. Furthermore, the reduced dimensionality also enhances the binding energy from  $\sim 4$  meV in bulk GaAs to up to four times that in GaAs QWs [17, 18]. Rather than the continuum of the joint density of states of valence and conduction band discussed previously, excitons are discrete states whose energy is lower than the band gap energy by the binding energy,  $E_X = E_g - E_b$ . Next, I discuss the influence of an electric field on excitons. For this, we return to undoped structures for simplicity.

## 7.2 The quantum-confined Stark effect

Consider the electron-hole pair in bulk GaAs in the co-moving frame of the hole. The hole generates the Coulomb potential

$$V(r) = \frac{e}{4\pi\epsilon_0\epsilon_r|r|}, \quad (7.7)$$

where  $\epsilon_r = 13.3$  is the relative permittivity of GaAs at low temperatures, which attracts the electron by the Coulomb energy  $E(r) = qV(r) = -eV(r)$ . Figure 7.2 depicts the Coulomb potential in magenta and the bound electron's wavefunction sketched in black. The electron-hole separation  $r$  is shown in units of the exciton Bohr radius in two dimensions [19]

$$a_B = \frac{2\pi\epsilon_0\epsilon_r\hbar^2}{\mu e^2} = 6 \text{ nm} \quad (7.8)$$

with  $\mu$  the reduced effective mass of conduction and heavy-hole valence bands.

We now apply an electric field  $F$ . This modifies the potential seen by the electron by  $erF$  as sketched in green Figure 7.2. Ignoring changes to the electron wavefunction, we can see that the electron can tunnel out of the Coulomb potential, leading to *field-induced ionization* of the exciton. Now place the exciton in a QW instead of in bulk with the electric field pointed such that it is out-of-plane of the QW. The field still tilts the potential, but because electrons and holes are confined into a quasi-two-dimensional plane, they cannot escape and hence do not dissociate. This is the quantum-confined Stark effect (QCSE) [20].

In order to obtain a qualitative understanding of the QCSE, consider an undoped GaAs/Al<sub>0.33</sub>Ga<sub>0.66</sub>As QW of width  $L = 20$  nm. We take a 57:43 ratio for the band offsets [15], resulting in discontinuities of height  $\Delta E_c = 0.24$  eV and  $\Delta E_{hh} = 0.18$  eV at the interfaces for the conduction and the heavy-hole valence band, respectively, and  $m_c^*/m_e = 0.067$  and  $m_{hh}^*/m_e = 0.34$  for the effective masses.<sup>4</sup> Assuming an infinitely deep well for simplicity, the eigenenergies are

$$E_n = \frac{1}{2m^*} \left[ \frac{\pi\hbar n}{L} \right]^2 \quad (7.9)$$

and the eigenstates are

$$\psi_n(z) = \sqrt{\frac{2}{L}} \sin\left(\frac{n\pi z}{L}\right). \quad (7.10)$$

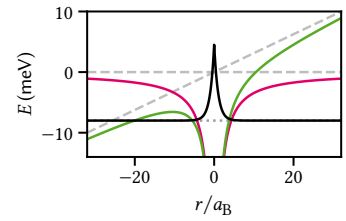


**Figure 7.2:** Effect of an in-plane electric field on an exciton wavefunction. In the hole's reference frame, the electron sees a static attractive Coulomb potential (magenta), resulting in a bound state (dotted gray line, wave function sketched in black). Applying an electric field ( $F = 100$  mV/ $\mu\text{m}$ , dashed gray lines) tilts the Coulomb potential (green) and leads to a transparent barrier through which the electron can tunnel out.

4: I note that the literature knows many different values for the hole effective mass in the plane of a quantum well, suggesting that one should actually measure it to be confident in the actual value.

The ground state energy is then 14 meV (3 meV) above the band edge, corresponding to 6 % (2 %) of the respective band offsets and implying that the infinite-well approximation is acceptable,<sup>5</sup> while the first excited state lies 42 meV higher than the ground state. The upper panel of Figure 7.3 depicts the first two wavefunctions of electrons and holes in a band structure diagram. Due to the symmetry of the confining potential, the wavefunctions are symmetric around the center of the well.

Now, applying an out-of-plane electric field tilts the bands and pulls electrons and holes to opposite interfaces of the QW. The Hamiltonian for the electrons in this case reads [16, 21, 22]

$$H = -\frac{\hbar^2}{2m^*} \frac{d^2}{dz^2} + eFz \quad (7.11)$$

if we take  $z$  to be zero at an interface and choose  $F \geq 0$ . Introducing the length and energy scales [16]

$$\tilde{\epsilon} = \left[ \frac{(\hbar e F)^2}{2m^*} \right]^{\frac{1}{3}}, \quad (7.12)$$

$$\tilde{z} = \left[ \frac{\hbar^2}{2m^* e F} \right]^{\frac{1}{3}} = \frac{\tilde{\epsilon}}{eF}, \quad (7.13)$$

and defining

$$Z_n(z) = z/\tilde{z} - \epsilon_n/\tilde{\epsilon} \quad (7.14)$$

with  $\epsilon_n$  the eigenvalues of  $H$ , the Schrödinger equation becomes [21]

$$\frac{d^2}{dZ_n^2} \psi_n(Z_n) = Z_n \psi_n(Z_n). \quad (7.15)$$

Equation 7.15 is known as the Stokes or Airy equation and has the general solution

$$\psi_n(Z_n) = \alpha_n \text{Ai}(Z_n) + \beta_n \text{Bi}(Z_n), \quad (7.16)$$

where  $\text{Ai}(z)$  and  $\text{Bi}(z)$  are the Airy functions.  $\text{Ai}(z)$  and  $\text{Bi}(z)$  oscillate for  $z < 0$  and decay (grow) exponentially for  $z > 0$ , respectively. As we assumed infinitely high barriers at  $z = 0$  and  $z = L$ , the boundary conditions impose

$$\psi_n(Z_n(0)) = \psi_n(Z_n(L)) = 0, \quad (7.17)$$

which completely determines the eigenstates and -energies. For large well widths or fields ( $eFL/\epsilon_n \gg 1$ ), the second term is exponentially suppressed and the eigenenergies are given by the zeros of  $\text{Ai}(Z_n)$ . For zero field, one recovers the square well solution (Equations 7.9 and 7.10).

The finite-field case is shown in the lower panel of Figure 7.3 for  $F = 5 \text{ V}/\mu\text{m}$ . Due to the larger effective mass of the heavy holes, the characteristic length scale  $\tilde{z}$  is shorter and hence the corresponding wavefunctions are narrower than their electronic counterparts. The ground state transition energy at this field is 10 meV below the gap or 27 meV lower than in the zero-field case.

For a full quantitative accounting of the transition energies, the exciton binding energy as well as finite barrier heights would need to be included. The former is on the order of 6 meV to 9 meV in GaAs and becomes smaller as the overlap of the electron and hole wavefunctions is reduced when applying an electric field, pulling the wavefunctions to opposite interfaces [20]. Miller et al. [22] found that finite-well properties could be reproduced by using effective well widths with infinite well

5: In a finite well, the wavefunctions decay exponentially into the barriers and result in slightly lower eigenenergies. However, the qualitative behavior remains the same.

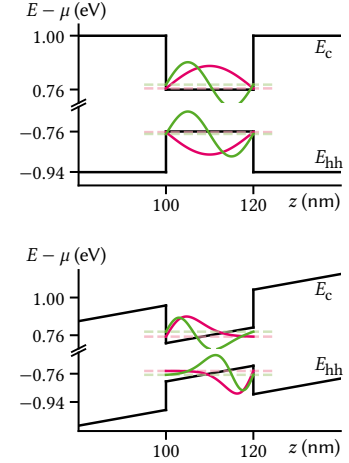


**Figure 7.3:** QCSE in an undoped QW. Top: conduction and heavy-hole valence band profiles along the growth direction. The wavefunctions of the first two eigenstates in the well are drawn in magenta and green, respectively. The ground state transition is larger by  $\Delta E = 17 \text{ meV}$  than the gap  $E_g$  due to the confinement. Bottom: same structure as above with an out-of-plane electric field applied across the structure ( $F = 5 \text{ V}/\mu\text{m}$ ). Analytical wavefunctions in the infinite-well approximation are shown in magenta and green again. The wavefunctions get pushed to opposite interfaces of the QW, lowering the ground state transition energy by  $\Delta E = -10 \text{ meV}$ . Excitonic effects are not included.

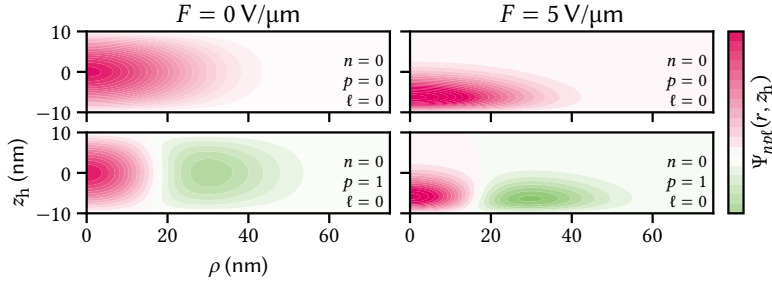


**Figure 7.4:** Center-of-mass exciton wavefunction (hole sector) in a harmonic trap under an electric field. Left column shows the zero-field and right column the high-field case. Top row is the ground state and bottom row the first excited state in the plane. The out-of-plane wavefunction is the ground state in all cases ( $n = 0$ ) and the trap confinement strength  $\omega/2\pi = 738$  GHz [8, Sec. 2.2.2].

models. The latter should have a small effect on the ground state energy as argued above.

### 7.2.1 In-plane confinement

So far, we have considered the QCSE in a single dimension, as if we were to apply a global electric field. However, as we saw before, the field lowers the exciton energy below the QW confinement and hence, if applied locally, results in an effective confinement potential in the plane of the QW. Descamps [8] performed numerical simulations for a geometry with circular gate electrodes with 200 nm diameter on both sides of a membrane, finding a confinement depth of 20 meV at  $F = 5$  V/ $\mu\text{m}$  that is well approximated by a single-particle harmonic potential with confinement strength  $\omega/2\pi = 738$  GHz corresponding to an oscillator length  $\xi = \sqrt{\hbar/M\omega} = 20$  nm.

How does this in-plane confinement modify the wavefunction? The harmonic potential applies to the center-of-mass wavefunction of the exciton with mass  $M = m_c^* + m_{hh}^*$ . We ignore the relative motion of electron and hole as the optical properties of the exciton are dominated by the behavior at zero separation for  $a_B/\xi < 1$  [23], and consider only  $\Delta n = 0$  transitions, *i. e.*, electron and hole in the same  $z$  quantum state, as  $\Delta n \neq 0$  transitions are much weaker [16]. Let us further initially assume a separable wavefunction and choose cylindrical coordinates according to the symmetry of the potential. We then have

$$\Psi_{npl}(z_e, z_h, \rho, \phi) = \psi_n(z_e)\psi_n(z_h)\chi_{pl}(\rho)\exp(i\ell\phi) \quad (7.18)$$

where<sup>6</sup> [24]

$$\chi_{pl}(\rho, \phi) = \sqrt{\frac{2p!}{2\pi\xi^2(p+|\ell|)!}} \exp(-\tilde{\rho}^2/2) \tilde{\rho}^{|\ell|} L_p^{|\ell|}(\tilde{\rho}) \quad (7.19)$$

with the associated Laguerre polynomial  $L_p^{|\ell|}(x)$  and we used the shorthand  $\tilde{\rho} = \rho/\xi$ . The numbers  $p \in \mathbb{N}$  and  $\ell \in \mathbb{Z}$  denote the principal and orbital momentum quantum numbers. The eigenenergies of the harmonic oscillator solution Equation 7.19 are given by

$$\epsilon_{p\ell} = \hbar\omega(2p + |\ell| + 1). \quad (7.20)$$

To account for a finite well width ( $L \approx \xi$  in our case), we can to a first approximation perform the replacement  $\rho \rightarrow r = \sqrt{\rho^2 + z^2}$  in Equation 7.18. The resulting wavefunction  $\Psi_{npl}(r, z_h)$  at fixed electron coordinate  $z_e$  is shown in Figure 7.4 for  $n = \ell = 0$  (which makes it independent of  $\phi$ ).

6: Note that Karimi et al. miss a factor  $2\pi$  in the normalization.

At last, we can use the exciton wavefunction  $\Psi_{nml}(r, \phi, z_e, z_h)$  to estimate the *oscillator strength*, a quantity often quoted in semiconductor spectroscopy. The oscillator strength puts in relation the quantum mechanical transition rate with the emission rate of a classical oscillator with frequency  $\omega = \Delta E/\hbar$  matching the transition energy [25]. For a dipole transition from state  $|i\rangle$  to state  $|j\rangle$ , it may be written as [16]

$$f_{ji} = \frac{2\mu\Delta E_{ji}}{\hbar^2} |\langle j|\mathbf{r}|i\rangle|^2, \quad (7.21)$$

where  $\mu$  is the reduced mass of the exciton. As the selection rules only allow in-plane dipole transitions for heavy holes, we write [23]

$$f_{np\ell} = \frac{2\mu\Delta E_{np\ell}}{\hbar^2} J_\phi^2 J_\rho^2 |\langle u_c|x|u_{hh}\rangle|^2 \quad (7.22)$$

for transitions with  $\Delta n = \Delta p = \Delta \ell = 0$ , where

$$J_r = \int_0^L dz \int_0^\infty d\rho \rho \psi_n^{(e)}(z) \psi_n^{(h)}(z) \chi_{p\ell}(\sqrt{\rho^2 + z^2}), \quad (7.23)$$

$$J_\phi = \int_0^{2\pi} d\phi \exp(i\ell\phi), \quad (7.24)$$

and  $|u_{c(hh)}\rangle$  are the Bloch functions of the valence and conduction band, respectively, that we have neglected so far. From Equation 7.24, we immediately see that the oscillator strength of states with nonzero orbital momentum ( $\ell \neq 0$ ) vanishes,  $f_{np0} = 0$ ! This in turn implies from Equation 7.20 that the exciton level spacing in a radially symmetric trap is given by  $\Delta E_n = 2\hbar\omega = 1$  meV, a factor two larger than assumed by Reference 8.

Figure 7.5 summarizes the QCSE in a QW additionally confined in the plane by local electric fields. The top panel shows the exciton transition energy  $\Delta E_{np}$  for  $\Delta n = \Delta p = 0$  in solid lines.<sup>7</sup> The first three in-plane sublevels due to the harmonic potential are drawn in less saturated colors but hard to see because the level spacing is much smaller than the out-of-plane subband spacing,  $\sim 1$  meV/50 meV. The ground state shows the expected quadratic dependence on the electric field also obtained, for example, from perturbation theory. Drawn as a dashed line is the induced dipole moment,

$$\mathbf{p}_{np}(F) = \frac{\partial \Delta E_{np}}{\partial F} \hat{\mathbf{e}}_z, \quad (7.25)$$

which is monotonously decreasing for the ground state as function of electric field  $F$ , consistent with a continuous lowering of energy. For the first excited state, the induced dipole moment is actually positive below  $2$  V/ $\mu\text{m}$ , leading to a repulsive interaction and hence a raising of the transition energy by up to  $1$  meV. The lower panel shows the oscillator strength, Equation 7.22, normalized to its value of the ground state at zero field,  $f_{00}(F=0)$ . It decays exponentially with the electric field as the overlap between electron and hole wavefunctions, which decay exponentially into the QW themselves, is reduced. Higher sublevels of the QW ground state (magenta, decreasing saturation) vary slightly in magnitude but show the same qualitative behavior while the first excited QW state (green) vanishes at a finite field before increasing again, in line with the behavior of the wavefunction, which has a node close to the center of the QW. Finally, the green dashed line shows the estimated tunneling probability (Equation 7.26) of the electron excited state. Tilting the QW results

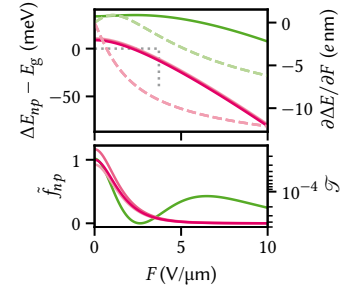


**Figure 7.5:** Electric field dependence of the QCSE for the first two energy levels in the QW. Top: the ground state energy (magenta) shows the expected quadratic dependence; the confinement energy is compensated at around  $F = 3.7$  V/ $\mu\text{m}$ . Dashed lines (right axis) show the derivative, revealing that the excited state is actually raised in energy at low fields. Bottom: oscillator strengths (same color code as above). Despite the fact that the wavefunctions are pulled apart by the electric field, the oscillator strength of the ground state has a maximum at around  $2.5$  V/ $\mu\text{m}$ . Dashed lines (right axis) show the tunneling probability through the barrier. Only the excited electron state is appreciably non-zero at large fields.

7: Note again that we neglected the exciton binding energy, which decreases with increasing field and hence slightly reduce the dispersion [20].



in a finite probability for the charge carriers confined within the well to escape as – for infinitely thick barriers – lower-lying states become available at some distance away, an effect known as Fowler-Nordheim tunneling. Following Reference 16, we can estimate the tunneling probability as

$$\mathcal{T}_n(F) \approx \exp \left\{ -\frac{\sqrt{4m^*[\Delta E_{c(hh)} - \epsilon_n]^3}}{\hbar e F} \right\}, \quad (7.26)$$

where  $\Delta E_{c(hh)}$  is the conduction (valence) band offset. Even at very large fields it remains below 1 % while the other states have a smaller probability still at below 1 ‰, suggesting that tunneling out of the well can be neglected at reasonably small fields. For doped structures, this conclusion may need to be revisited as remote dopants pull the conduction band edge down and thus narrow the tunneling barrier to the QW.

### 7.3 Excitonic complexes

If we liken the exciton to a Hydrogen atom<sup>8</sup> with modified binding energy  $E_b$  and Bohr radius  $a_B$ , it is natural to expect molecules and ions of these states to exist. The simplest molecule, or excitonic complex, is the biexciton, the analog of the  $H_2$  molecule. Following a similar argument as for the binding energy of the exciton, we expect that of the biexciton to also increase as the dimensionality of the system is reduced. Indeed, in QWs it has been measured to be on the order of 1 meV, 3 to 4 times larger than in 3D [26], although also negative binding energies, corresponding to an anti-bonding state, have been reported [27–29]. A signature of biexcitons is the power dependence of their photoluminescence (PL). The steady-state density of electron-hole pairs, which is proportional to the exciton density at low enough powers, is proportional to the irradiance, *i. e.*, the excitation power. Conversely, the probability to form a two-body bound state is proportional to the square of the density of those bodies and we hence expect the power under the PL peak of a biexciton emission to be proportional to the square of the laser power used to excite the sample.

Besides the neutral biexciton, there exist also charged states consisting of three or more bodies. Here, additional electrons or holes bind to an exciton, forming negative or positively charged trions similar to  $H^-$  or  $He^+$  ions. Naturally, this process is favored when a large number of surplus charge carriers is present in the sample such as is the case in doped QWs with a 2DEG (or two-dimensional hole gas (2DHG)). In these structures, the trion binding energy has been found to also be on the order of 1 meV [30, 31].

8: Although positronium is a better analogon.

# The mjolnir measurement framework

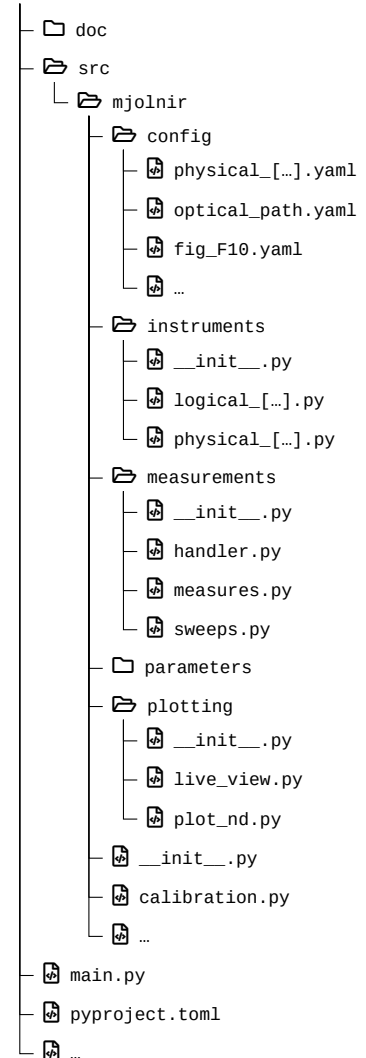


**Figure 8.1:** Source tree structure of the mjolnir package. Logical QCoDeS instruments and parameters are defined in the instruments and parameters modules, respectively. Instruments are configured using yaml files located in the config directory. The measurements module provides classes for the abstraction of measurements using QCoDeS underneath. Live plots of instrument data as well as a plot function for multidimensional measurement data are defined in the plotting module. calibration.py contains routines for power, CCD, and excitation rejection calibrations. The main.py file is a code cell-based script that serves as the entrypoint for measurements.

## 9.1 Transfer-matrix method simulations of the membrane structure

The transfer-matrix method (TMM) is a computationally efficient method of obtaining the electric field in layered structures. In this section, I perform simulations of the heterostructure membranes investigated in this part of the present thesis using the PyMoosh package [32] to elucidate the observed quenching of PL when illuminating gate electrodes as well as the overall optical efficiency.<sup>1</sup> I will first briefly recap the simulation method following Reference 32. For more details, refer to *ibid.* and references therein.

Consider a layered structure along  $z$  with interfaces at  $z_i, i \in \{0, 1, \dots, N+1\}$  that is translationally invariant along  $x$  and  $y$ . Each layer  $i$  may consist of a different dielectric material characterized by a (complex) relative permittivity  $\epsilon_{r,i}$ .<sup>2</sup> The electric field component along  $y$  of an electromagnetic wave transverse electric (TE) mode originating in some far away point satisfies the Helmholtz equation

$$\frac{\partial^2 E_y}{\partial z^2} + \gamma_i^2 E_y = 0, \quad (9.1)$$

where  $\gamma_i = \sqrt{\epsilon_{r,i} k_0^2 - k_x^2}$  with  $k_0 = \omega/c$  the wave vector in vacuum and  $k_x$  the component along  $x$ . In layer  $i$  of the structure, the solution to Equation 9.1 may be written as a superposition of plane waves incident and reflected on the lower and upper interfaces [32],

$$\begin{cases} E_{y,i}(z) = A_i^+ \exp\{i\gamma_i[z - z_i]\} + B_i^+ \exp\{-i\gamma_i[z - z_i]\}, \\ E_{y,i}(z) = A_i^- \exp\{i\gamma_i[z - z_{i+1}]\} + B_i^- \exp\{-i\gamma_i[z - z_{i+1}]\}, \end{cases} \quad (9.2)$$

where the coefficients with superscript  $+$  ( $-$ ) are referenced to the phase at the upper (lower) interface, respectively. Matching these solutions at  $z = z_i$  for all  $i$  to satisfy the interface conditions imposed by Maxwell's equations gives rise to a linear system of equations, the solution to which can be obtained through several different methods.

A particularly simple method is the transfer-matrix method ( $T$ -matrix formalism), which corresponds to writing the interface conditions at  $z = z_i$  as the matrix equation

$$\begin{pmatrix} A_{i+1}^+ \\ B_{i+1}^+ \end{pmatrix} = T_{i,i+1} \begin{pmatrix} A_i^- \\ B_i^- \end{pmatrix} \quad (9.3)$$

with

$$T_{i,i+1} = \frac{1}{2\gamma_{i+1}} \begin{pmatrix} \gamma_i + \gamma_{i+1} & \gamma_i - \gamma_{i+1} \\ \gamma_i - \gamma_{i+1} & \gamma_i + \gamma_{i+1} \end{pmatrix} \quad (9.4)$$

the transfer matrix for interface  $i$ . Connecting the coefficients for adjacent interfaces within a layer of height  $h_i = z_{i+1} - z_i$  requires propagating

1: Strictly speaking, the term TMM only refers to one of the several formalisms implemented in the PyMoosh package. While fast, it is not the most numerically stable, and other methods may be preferred if wall time is not a limiting issue.

2: We disregard magnetic materials with relative permeability  $\mu_r \neq 1$  for simplicity.

the phase,

$$\begin{pmatrix} A_i^- \\ B_i^- \end{pmatrix} = C_i \begin{pmatrix} A_i^+ \\ B_i^+ \end{pmatrix}, \quad (9.5)$$

with

$$C_i = \exp \{ \text{diag}(-i\gamma_i h_i, i\gamma_i h_i) \}. \quad (9.6)$$

Iterating Equations 9.4 and 9.6, the total transfer matrix  $T = T_{0,N+1}$  then reduces to the matrix product

$$T = T_{N,N+1} \prod_{i=0}^{N-1} T_{i,i+1} C_i. \quad (9.7)$$

From  $T$ , the reflection and transmission coefficients can be obtained as  $r = A_0^- = -T_{01}/T_{00}$  and  $t = B_{N+1}^+ = rT_{10} + T_{11}$ . Taking the absolute value square of reflection and transmission coefficients then yields the reflectance  $\mathcal{R}$  and the transmittance  $\mathcal{T}$ , which correspond to the fraction of total incident power being reflected and transmitted, respectively. To obtain the absorptance  $\mathcal{A}$ , the fraction of power being absorbed, in layer  $i$ , one can compute the difference of the  $z$ -components of the Poynting vectors (*cf.* Equation 3.18) at the top of layers  $i$  and  $i+1$ . In the TE case considered here, Equation 3.18 reduces to [32]

$$S_i = \text{Re} \left[ \frac{\gamma_i^*}{\gamma_0} (A_i^+ - B_i^+)^* (A_i^+ + B_i^+) \right] \quad (9.8)$$

and is hence straightforward to extract from the calculation of either the  $S$  or  $T$  matrices.

Equation 9.7 is simple to evaluate on a computer, making this method attractive for numerical applications. However, the opposite signs in the argument of the exponentials in Equation 9.6 can lead to instabilities for evanescent waves ( $\gamma_i \in \mathbb{C}$ ) due to finite-precision floating point arithmetic [33]. Rewriting Equation 9.4 to have incoming and outgoing fields on opposite sides of the equality alleviates this issue while sacrificing the simple matrix-multiplication composition rule in what is known as the scattering matrix ( $S$ -matrix) formalism. Finally, note that for a thorough accounting of in- and out-going field amplitudes, excitonic effects should be included, for example using the approach by D'Andrea and Del Sole [34].

Beyond the calculation of the aforementioned coefficients, the TMM formalism also allows to compute the full spatial dependence of the fields. Two cases are implemented in PyMoosh: irradiation of the layered structured with a Gaussian beam rather than plane waves of infinite extent, and a current line source inside the structure. In the first case, the previously assumed translational invariance along  $x$  leading to a plane-wave spatial dependence is replaced by a superposition of plane waves weighted with a normally distributed amplitude,<sup>3</sup>

$$E_{y,i}(x, z) = \exp(ik_x x) \rightarrow \int \frac{dk_x}{2\pi} \mathcal{E}_0(k_x) E_{y,i}(k_x, z) \exp(ik_x x), \quad (9.9)$$

with (*cf.* Equation 4.6)

$$\mathcal{E}_0(k_x) = \frac{w_0}{2\sqrt{\pi}} \exp \left\{ -ik_x x_0 - \left[ \frac{w_0 k_x}{2} \right]^2 \right\} \quad (9.10)$$

3: *I.e.*, the inverse Fourier transform of  $\mathcal{E}_0(k_x) E_{y,i}(k_x, z)$ .

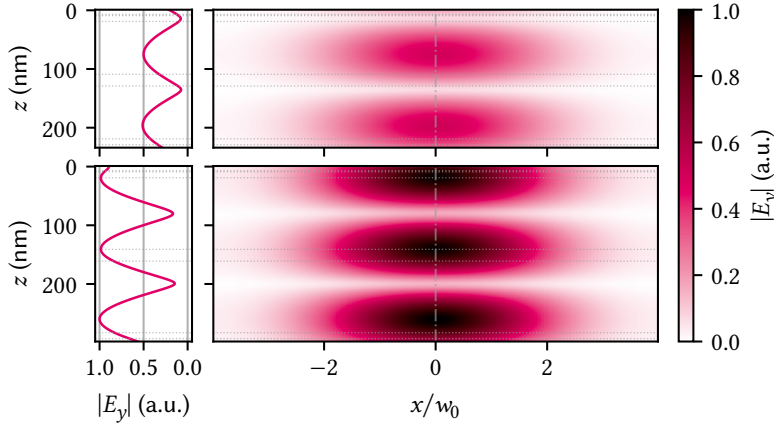


**Figure 9.1:** Absolute value of the electric field inside the double-gated heterostructure under illumination with a Gaussian beam at  $\lambda = 825$  nm from the top. Top (bottom) panels show the structure with the default (optimized) barrier thickness of 90 nm (122 nm), respectively. Dotted horizontal lines indicate interfaces between different materials while the vertical dash-dotted line indicates the position of the line cuts shown in the left column. Increasing the thickness of the barrier has two beneficial effects; first, the overall field intensity inside the structure is higher by a factor of two, and second, there is a peak rather than a knot in the QW at a depth of  $\sim 120$  nm ( $\sim 150$  nm), leading to enhanced absorption.

and

$$E_{y,i}(k_x, z) = A_i^- \exp\{i\gamma_i(k_x)[z - z_{i+1}]\} + B_i^+ \exp\{-i\gamma_i(k_x)[z - z_i]\}, \quad (9.11)$$

and where we considered only normal incidence for simplicity.

In the second case, Langevin et al. [32] consider an AC current  $I$  flowing through a translationally invariant, one-dimensional wire along  $y$  at  $x = x_s$ . This introduces a source term into the Helmholtz equation Equation 9.1 which, upon Fourier transforming in  $x$  direction, leads to

$$\frac{\partial^2 \hat{E}_y}{\partial z^2} + \gamma_i^2 \hat{E}_y = -i\omega\mu_0 I \delta(z) \exp(ik_x x_s). \quad (9.12)$$

The electric field  $\hat{E}_{y,i}(k_x, z)$  is thus proportional to the Green's function of Equation 9.12 and can be obtained using a similar procedure as in the case of a distant source incident on the structure by matching the interface conditions. Performing the inverse Fourier transform by means of Equation 9.9 with constant weights,  $\mathcal{E}_0(k_x) \equiv 1$ , then yields the two-dimensional spatial distribution of the electric field,  $E_{y,i}(x, z)$ .

**Table 9.1:** Absorptance  $\mathcal{A}$  and reflectance  $\mathcal{R}$  in the QW for different configurations of the heterostructure. “Bare” is the standard structure without gate electrodes. “TG” and “BG” are with a gate on either the top or bottom side. “TG+BG” is with gates on both sides as on a trap site.

	$\mathcal{A}$ (%)	$\mathcal{R}$ (%)
Bare	2.9	22.4
TG	1.8	42.0
BG	0.5	82.7
TG+BG	0.4	84.8

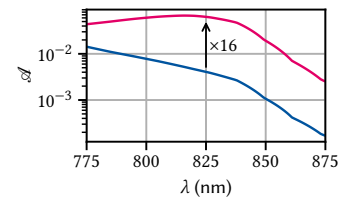


**Figure 9.2:** QW absorptance  $\mathcal{A}$  in a heterostructure with default (blue) and optimized (magenta) barrier thickness and top and bottom gates as function of wavelength. Optimization was performed at 825 nm using the differential evolution algorithm implemented in PyMoosh, resulting in a barrier thickness of 122 nm and an absorptance better by a factor of 16 at 825 nm.

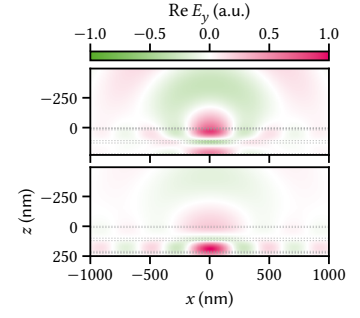


**Figure 9.3:** Real part of the electric field emitted by a current line located in the QW (black point) for different cases of the unoptimized structure. From top to bottom: bare heterostructure, top gate, bottom gate, top and bottom gate. The half space  $z < 0$  is the air above the membrane in the direction of the objective lens and the dotted lines indicate interfaces between materials. Evidently, the bottom gate reduces the amplitude in the upper half of the membrane and thereby the outcoupling efficiency compared to the structures with just a top gate, consistent with what is observed in the experiment.

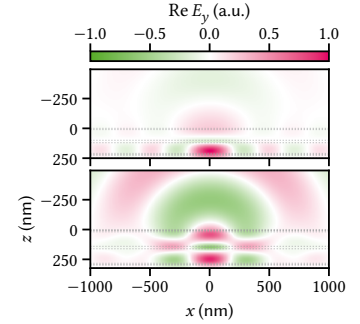


**Figure 9.4:** Real part of the electric field emitted by a current line located in the QW (black point) for the default (top) and optimized (bottom) structures with top and bottom gates. Optimizing the barrier thickness for absorption in the QW evidently also drastically improves the outcoupling efficiency into the half-space  $z < 0$ .

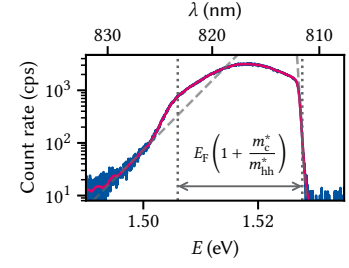
Figure 9.5 shows a typical PL spectrum obtained on the bare, unbiased QW of a doped membrane sample. This measurement corresponds to the configuration already discussed in Figure 7.1. Electrons require an energy of at least  $E_F$  and, because of the vanishingly small photon momentum, a momentum of at least  $k_F$  to be excited into a free state above the Fermi level  $\mu$  (dotted gray line). Once excited, they quickly relax down to the Fermi edge at  $\mu$  from where they can recombine emitting a photon. As the Fermi sea is at a finite temperature, the high-energy shoulder of the PL spectrum is hence thermally broadened according to the Fermi distribution function of the electron gas (dashed gray line). The associated temperature is on the order of a few Kelvin and hence orders of magnitude higher than the lattice temperature of 10 mK. This effect has already been observed by Pinczuk et al. [35]. Like in those experiments, the temperature of the Fermi edge does not vary significantly with excitation power, making carrier heating due to high excitation power an unlikely cause [36].

PL emission is possible also at lower energies as electrons inside the Fermi sea recombine with the free photo-hole that scatters towards the valence band edge. The band gap then defines the low-energy shoulder of the PL spectrum, below which there are – ideally – no states available (dotted gray line). However, the PL reveals there are indeed free states decaying exponentially into the gap, originating most likely from impurities (dashed gray line). Compared to the results of Kamburov et al. [14], the PL spectra obtained here are much flatter over energy, with the PL peak typically close to the middle between gap and Fermi edge. Conversely, Kamburov et al. [14] observed a strong peak at the band gap, indicating that in our samples either hole scattering rates are smaller and recombination more often takes place before the photo-hole fully relaxed to the valence band edge, or holes are more strongly localized and therefore have a wider spread in  $k$ -space, enabling transitions in a wider range of wave vectors [37].

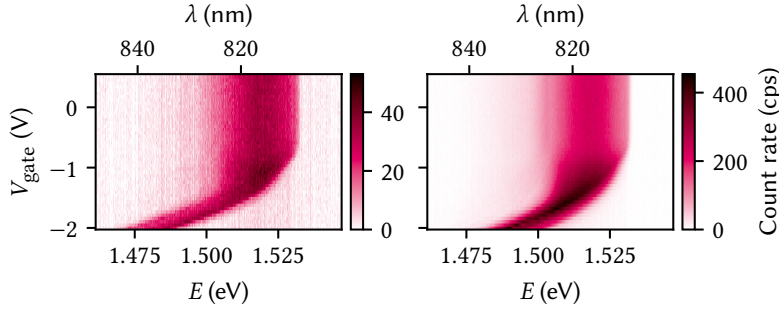
From the width of the 2DEG emission, we can calculate the charge carrier density by relating it to the Fermi energy in two dimensions [1, 35],

$$n = \frac{m_c^* E_F}{\pi \hbar^2} = \frac{\mu \Delta E}{\pi \hbar^2}, \quad (9.13)$$

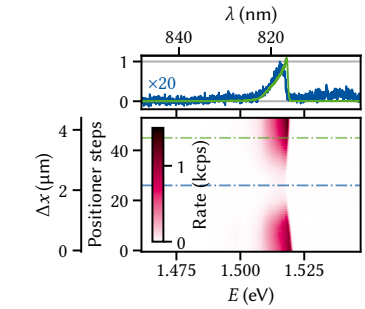
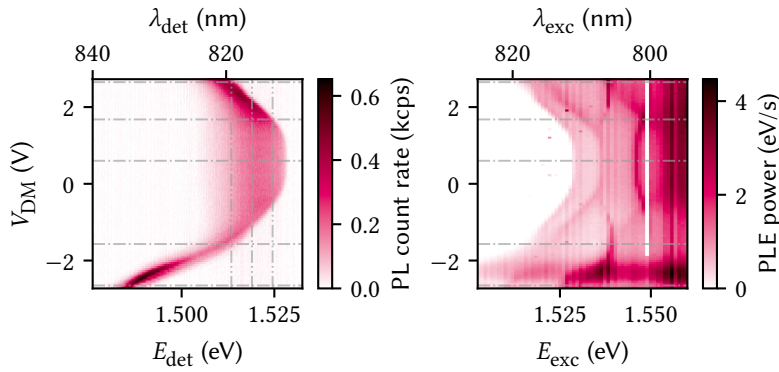
where  $\Delta E$  is the bandwidth of the emission (dashed gray lines in Figure 9.5) and  $\mu = m_c^* m_{hh}^* / (m_c^* + m_{hh}^*)$  is the reduced mass of conduction and valence band. For this particular sample, Equation 9.13 yields  $n = 5 \times 10^{11} \text{ cm}^{-2}$ . Finally, we observe that the gap according to the preceding analysis is redshifted from the undoped bulk gap of 1.519 eV by 13 meV. Descamps [8] hypothesized that the removal of the GaAs substrate and the associated change in strain leads to this lowering of the band gap. However, this effect was also already observed by Pinczuk et al. [35] in “bulk” modulation-doped GaAs QWs. There, the authors put forth a renormalization of the band gap due to many-body interactions as an explanation. Indeed, it is likely just bandgap narrowing due to doping [38].



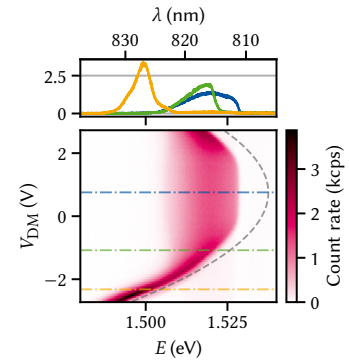
**Figure 9.5:** PL of the bare 2DEG. Magenta line is a smoothing spline fit to the data. Indicated by dotted gray lines are the Fermi edge at high and the band edge at low energy. The Fermi edge has a Fermi distribution (exponential indicated by a dashed gray line) whose temperature is typically much higher than the lattice temperature ( $\sim 1$  K). Below the band edge there is an exponential tail (dashed gray line) due to impurities that permeates far into the gap.



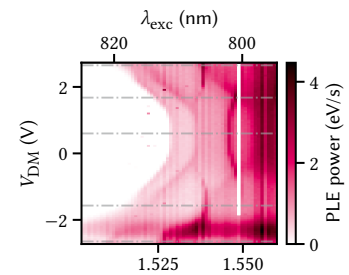
**Figure 9.6:** PL as function of gate voltage on a single fan-out gate on the bottom (left) and top (right) side of the membrane. The behavior is qualitatively similar but the overall quantum efficiency lower by an order of magnitude for gates on the bottom (as-grown buried) side.



**Figure 9.7:** PL of the unbiased QW as the laser is stepped across a bottom gate. The line traces in the upper panel are taken at the positions indicated by dashed-dotted lines. Positioner steps are converted to distance using a linear fit of the positioner readout after the initial hysteresis has worn off (about 10 steps). The Fermi edge shows a slight redshift when on top of the gate in this sample.



**Figure 9.8:** PL as function of difference-mode voltage on a large exciton trap. The observed Stark shift follows roughly the expected quadratic dispersion, but is offset by 0.75 V with respect to zero bias. Dashed gray line is a guide to the eye of a parabola with curvature  $-3.5 \text{ meV/V}^2$ . Line cuts in the upper panel are taken at the voltages indicated by dash-dotted lines in the lower.





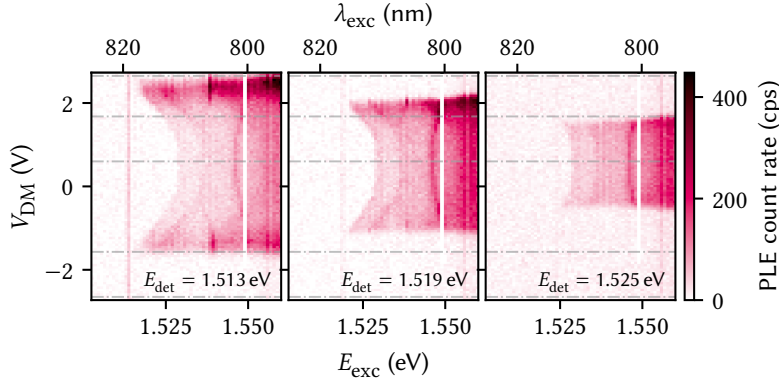
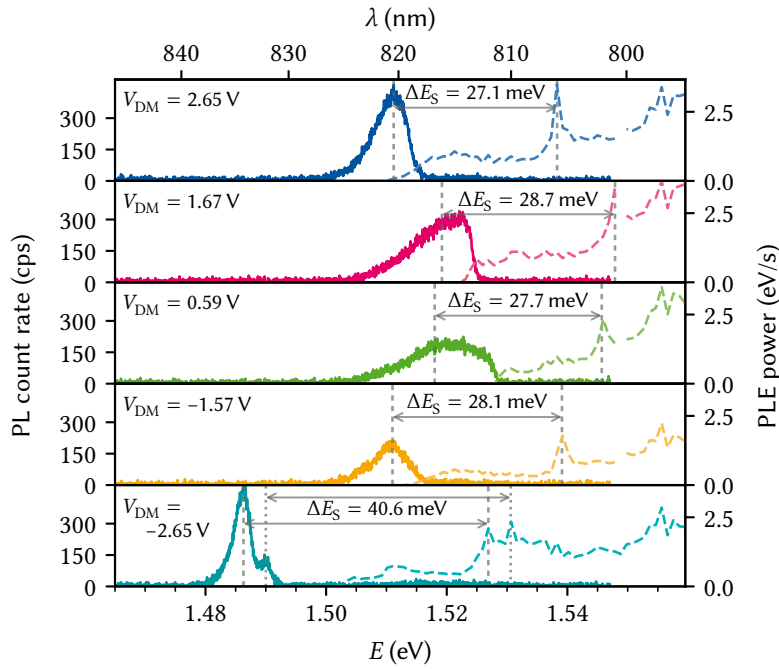


Figure 9.11



**Figure 9.12:** PL (solid lines) and photoluminescence excitation (PLE) (dashed lines) for different voltages  $V_{DM}$  (cf. Figure 9.8). The PLE data points correspond to PL spectra integrated up to the laser line. Arrows indicate the Stokes shift  $\Delta E_S$ , which is approximately constant (although assignment of the gap peak is difficult for 1.57 V and 0 V) until the 2DEG is fully depleted and the exciton resonance shifts quadratically with the electric field. The features at 1.555 eV do not shift with the voltage and are thus likely unrelated to the trap. For the largest voltage, there is another peak at 1.51 eV whose origin is unclear.

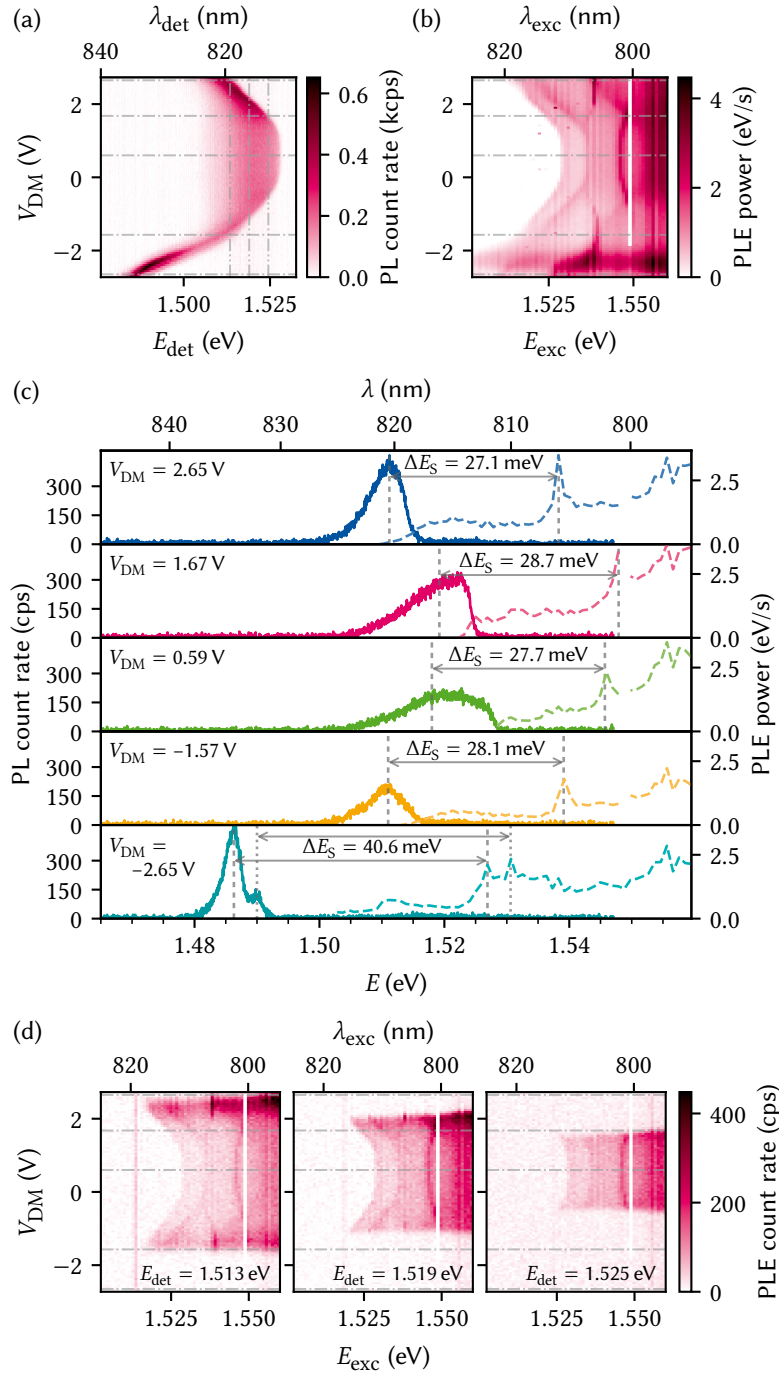
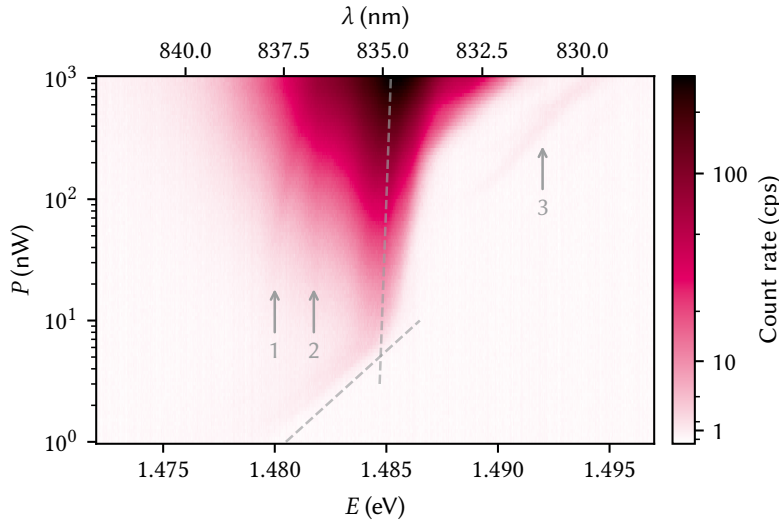
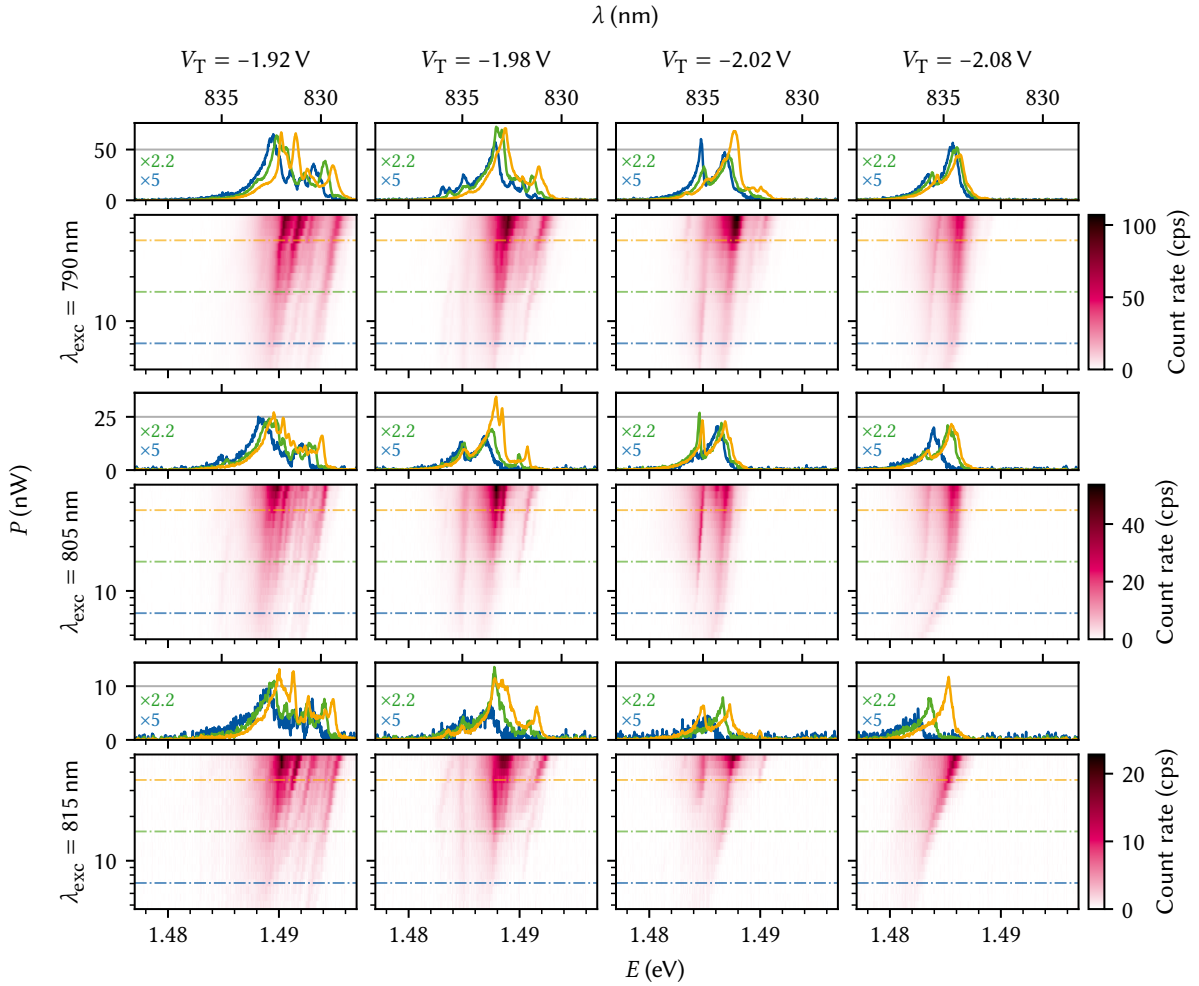


Figure 9.13



**Figure 9.14:** PL as function of excitation power  $P$  plotted on a logarithmic color scale. Two qualitatively different regimes are indicated by dashed gray lines as guides to the eye; below 10 nW, the main peak displays a blueshift logarithmic in excitation power,  $E = 1.485 \text{ eV} + 5 \text{ meV} \log_{10} P$ . Above, the blueshift diminishes significantly. Three additional lines, indicated by arrows, with varying power dispersion appear.



**Figure 9.15:** Wide-range PL parameter sweep on a large exciton trap plotted as function of excitation power and detection energy. Rows are data for three different excitation wavelengths, columns for four different top gate voltages  $V_T$  and share color and line cut scales. Line cuts are taken at the indicated positions of  $P = 7 \text{ nW}$ ,  $16 \text{ nW}$  and  $35 \text{ nW}$  and drawn scaled by the fraction of excitation power with respect to  $35 \text{ nW}$ .



## **Part IV**

# **A FILTER-FUNCTION FORMALISM FOR UNITAL QUANTUM OPERATIONS**

# **APPENDIX**

# Additional TMM simulations



## C.1 Dependence on epoxy thickness

## C.2 Optimization of the barrier thickness

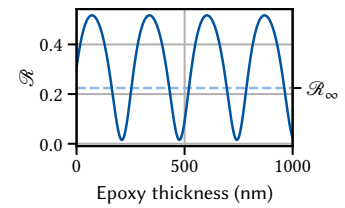


Figure C.1

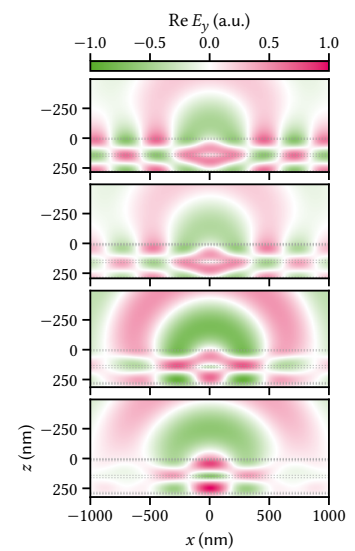


Figure C.2

# Bibliography

- [1] Thomas Ihn. *Semiconductor Nanostructures: Quantum States and Electronic Transport*. Oxford University Press, Nov. 26, 2009. (Visited on 01/25/2022) (cited on pages 34, 45).
- [2] Horst L. Stormer. “Nobel Lecture: The Fractional Quantum Hall Effect.” In: *Rev. Mod. Phys.* 71.4 (July 1, 1999), pp. 875–889. DOI: [10.1103/RevModPhys.71.875](https://doi.org/10.1103/RevModPhys.71.875). (Visited on 01/19/2022) (cited on page 34).
- [3] R. H. Harrell et al. “Fabrication of High-Quality One- and Two-Dimensional Electron Gases in Undoped GaAs/AlGaAs Heterostructures.” In: *Applied Physics Letters* 74.16 (Apr. 19, 1999), pp. 2328–2330. DOI: [10.1063/1.123840](https://doi.org/10.1063/1.123840). (Visited on 09/18/2023) (cited on page 34).
- [4] J. C. H. Chen et al. “Fabrication and Characterization of Ambipolar Devices on an Undoped AlGaAs/-GaAs Heterostructure.” In: *Appl. Phys. Lett.* 100.5 (Jan. 30, 2012), p. 052101. DOI: [10.1063/1.3673837](https://doi.org/10.1063/1.3673837). (Visited on 09/18/2023) (cited on page 34).
- [5] Hai-Ou Li et al. “Fabrication and Characterization of an Undoped GaAs/AlGaAs Quantum Dot Device.” In: *Journal of Applied Physics* 116.17 (Nov. 3, 2014), p. 174504. DOI: [10.1063/1.4900915](https://doi.org/10.1063/1.4900915). (Visited on 08/21/2023) (cited on page 34).
- [6] L. A. Tracy, T. W. Hargett, and J. L. Reno. “Few-Hole Double Quantum Dot in an Undoped GaAs/AlGaAs Heterostructure.” In: *Applied Physics Letters* 104.12 (Mar. 24, 2014), p. 123101. DOI: [10.1063/1.4868971](https://doi.org/10.1063/1.4868971). (Visited on 08/21/2023) (cited on page 34).
- [7] Matthias E Rößler. “Contacting Backgated Two-dimensional Electron Gases for Quantum Dot Spin Qubits in GaAs.” MA thesis. Aachen: RWTH Aachen University, Sept. 2016 (cited on page 34).
- [8] Thomas Descamps. “Electrostatic Exciton Trap in a Thin Semiconductor Membrane for Optical Coupling to a GaAs Spin Qubit.” PhD thesis. Aachen: RWTH Aachen University, 2021 (cited on pages 34, 37, 38, 45).
- [9] Sebastian Kindel. PhD thesis. Aachen: RWTH Aachen University, 2025 (cited on page 34).
- [10] Takafumi Fujita et al. “Distinguishing Persistent Effects in an Undoped GaAs/AlGaAs Quantum Well by Top-Gate-Dependent Illumination.” In: *Journal of Applied Physics* 129.23 (June 21, 2021), p. 234301. DOI: [10.1063/5.0047558](https://doi.org/10.1063/5.0047558). (Visited on 09/15/2022) (cited on page 34).
- [11] A. Shetty et al. “Effects of Biased and Unbiased Illuminations on Two-Dimensional Electron Gases in Dopant-Free GaAs/AlGaAs.” In: *Phys. Rev. B* 105.7 (Feb. 7, 2022), p. 075302. DOI: [10.1103/PhysRevB.105.075302](https://doi.org/10.1103/PhysRevB.105.075302). (Visited on 08/21/2023) (cited on page 34).
- [12] Huiyi Wang. “Stability Investigation of GaAs Quantum Dot Devices under Illumination.” MA thesis. Aachen: RWTH Aachen University, Nov. 4, 2023. 65 pp. (cited on page 34).
- [13] Maxim Reznikov. “Investigating Device Stability and Exploring New Materials for Semiconductor Spin Qubit Optical Interfaces.” MA thesis. Aachen: RWTH Aachen University, June 2024 (cited on page 34).
- [14] D. Kamburov et al. “Use of Micro-Photoluminescence as a Contactless Measure of the 2D Electron Density in a GaAs Quantum Well.” In: *Appl. Phys. Lett.* 110.26 (June 26, 2017), p. 262104. DOI: [10.1063/1.4985439](https://doi.org/10.1063/1.4985439). (Visited on 06/29/2022) (cited on pages 34, 45).
- [15] R. C. Miller, D. A. Kleinman, and A. C. Gossard. “Energy-Gap Discontinuities and Effective Masses for GaAs – Al<sub>x</sub>Ga<sub>1-x</sub>As Quantum Wells.” In: *Phys. Rev. B* 29.12 (June 15, 1984), pp. 7085–7087. DOI: [10.1103/PhysRevB.29.7085](https://doi.org/10.1103/PhysRevB.29.7085). (Visited on 06/30/2022) (cited on pages 34, 35).
- [16] John H. Davies. *The Physics of Low-Dimensional Semiconductors: An Introduction*. Cambridge: Cambridge Univ. Press, 2009. 438 pp. (cited on pages 34, 36–39).
- [17] Lucio Claudio Andreani and Alfredo Pasquarello. “Accurate Theory of Excitons in GaAs-Ga<sub>1-x</sub>Al<sub>x</sub>As Quantum Wells.” In: *Phys. Rev. B* 42.14 (Nov. 15, 1990), pp. 8928–8938. DOI: [10.1103/PhysRevB.42.8928](https://doi.org/10.1103/PhysRevB.42.8928). (Visited on 02/07/2024) (cited on page 35).
- [18] G. D. Gilliland. “Photoluminescence Spectroscopy of Crystalline Semiconductors.” In: *Mater. Sci. Eng. R Rep.* 18.3 (1997), pp. 99–399. DOI: [10.1016/S0927-796X\(97\)80003-4](https://doi.org/10.1016/S0927-796X(97)80003-4) (cited on page 35).
- [19] Thomas Olsen et al. “Simple Screened Hydrogen Model of Excitons in Two-Dimensional Materials.” In: *Phys. Rev. Lett.* 116.5 (Feb. 2, 2016), p. 056401. DOI: [10.1103/PhysRevLett.116.056401](https://doi.org/10.1103/PhysRevLett.116.056401). (Visited on 07/16/2025) (cited on page 35).



- [20] D. A. B. Miller et al. “Band-Edge Electroabsorption in Quantum Well Structures: The Quantum-Confined Stark Effect.” In: *Phys. Rev. Lett.* 53.22 (Nov. 26, 1984), pp. 2173–2176. doi: [10.1103/PhysRevLett.53.2173](https://doi.org/10.1103/PhysRevLett.53.2173). (Visited on 06/30/2022) (cited on pages 35, 36, 38).
- [21] A. Rabinovitch and J. Zak. “Electrons in Crystals in a Finite-Range Electric Field.” In: *Phys. Rev. B* 4.8 (Oct. 15, 1971), pp. 2358–2370. doi: [10.1103/PhysRevB.4.2358](https://doi.org/10.1103/PhysRevB.4.2358). (Visited on 06/26/2025) (cited on page 36).
- [22] D. A. B. Miller et al. “Electric Field Dependence of Optical Absorption near the Band Gap of Quantum-Well Structures.” In: *Phys. Rev. B* 32.2 (July 15, 1985), pp. 1043–1060. doi: [10.1103/PhysRevB.32.1043](https://doi.org/10.1103/PhysRevB.32.1043). (Visited on 06/30/2022) (cited on page 36).
- [23] A. V. Kavokin. “Exciton Oscillator Strength in Quantum Wells: From Localized to Free Resonant States.” In: *Phys. Rev. B* 50.11 (Sept. 15, 1994), pp. 8000–8003. doi: [10.1103/PhysRevB.50.8000](https://doi.org/10.1103/PhysRevB.50.8000). (Visited on 07/17/2025) (cited on pages 37, 38).
- [24] E. Karimi et al. “Radial Quantum Number of Laguerre-Gauss Modes.” In: *Phys. Rev. A* 89.6 (June 16, 2014), p. 063813. doi: [10.1103/PhysRevA.89.063813](https://doi.org/10.1103/PhysRevA.89.063813). (Visited on 07/17/2025) (cited on page 37).
- [25] Robert C. Hilborn. “Einstein Coefficients, Cross Sections,  $f$  Values, Dipole Moments, and All That.” In: *Am. J. Phys.* 50.11 (Nov. 1, 1982), pp. 982–986. doi: [10.1119/1.12937](https://doi.org/10.1119/1.12937). (Visited on 07/16/2025) (cited on page 38).
- [26] R. C. Miller and D. A. Kleinman. “Excitons in GaAs Quantum Wells.” In: *Journal of Luminescence* 30.1 (Feb. 1, 1985), pp. 520–540. doi: [10.1016/0022-2313\(85\)90075-4](https://doi.org/10.1016/0022-2313(85)90075-4). (Visited on 02/02/2024) (cited on page 39).
- [27] Satoshi Kako et al. “Biexciton in Single GaN/AlN Self-Assembled Quantum Dots.” In: *Conf. Lasers Electro-Opt. Quantum Electron. Conf. Photonic Appl. Syst. Technol.* International Quantum Electronics Conference. San Francisco, California: OSA, 2004, IThC5. doi: [10.1364/IQEC.2004.IThC5](https://doi.org/10.1364/IQEC.2004.IThC5). (Visited on 11/15/2024) (cited on page 39).
- [28] G.E. Dialynas et al. “Anti-Binding of Biexcitons in (211)B InAs/GaAs Piezoelectric Quantum Dots.” In: *Physica E: Low-dimensional Systems and Nanostructures* 40.6 (Apr. 2008), pp. 2113–2115. doi: [10.1016/j.physe.2007.10.036](https://doi.org/10.1016/j.physe.2007.10.036). (Visited on 11/15/2024) (cited on page 39).
- [29] S. Amloy et al. “Size Dependent Biexciton Binding Energies in GaN Quantum Dots.” In: *Appl. Phys. Lett.* 99.25 (Dec. 19, 2011), p. 251903. doi: [10.1063/1.3670040](https://doi.org/10.1063/1.3670040). (Visited on 11/15/2024) (cited on page 39).
- [30] Axel Esser et al. “Photoluminescence and Radiative Lifetime of Trions in GaAs Quantum Wells.” In: *Phys. Rev. B* 62.12 (Sept. 15, 2000), pp. 8232–8239. doi: [10.1103/PhysRevB.62.8232](https://doi.org/10.1103/PhysRevB.62.8232). (Visited on 06/30/2022) (cited on page 39).
- [31] Israel Bar-Joseph. “Trions in GaAs Quantum Wells.” In: *Semicond. Sci. Technol.* 20.6 (June 1, 2005), R29–R39. doi: [10.1088/0268-1242/20/6/R01](https://doi.org/10.1088/0268-1242/20/6/R01). (Visited on 07/03/2022) (cited on page 39).
- [32] Denis Langevin et al. “PyMoosh: A Comprehensive Numerical Toolkit for Computing the Optical Properties of Multilayered Structures.” In: *J. Opt. Soc. Am. B* 41.2 (Feb. 1, 2024), A67. doi: [10.1364/JOSAB.506175](https://doi.org/10.1364/JOSAB.506175). (Visited on 11/11/2024) (cited on pages 41–43).
- [33] Denny Dütz et al. “Distributed Bragg Reflectors for Thermal Isolation of Semiconductor Spin Qubits.” In preparation (cited on page 42).
- [34] A. D’Andrea and R. Del Sole. “Exciton Quantization and Polariton Propagation in Semiconductor Slabs: From Semi-Infinite Crystals to Quantum Wells.” In: *Phys. Rev. B* 41.3 (Jan. 15, 1990), pp. 1413–1423. doi: [10.1103/PhysRevB.41.1413](https://doi.org/10.1103/PhysRevB.41.1413). (Visited on 07/17/2025) (cited on page 42).
- [35] A. Pinczuk et al. “Optical Processes of 2D Electron Plasma in GaAs-(AlGa)As Heterostructures.” In: *Solid State Communications* 50.8 (May 1, 1984), pp. 735–739. doi: [10.1016/0038-1098\(84\)90975-X](https://doi.org/10.1016/0038-1098(84)90975-X). (Visited on 07/01/2022) (cited on page 45).
- [36] R. Ulbrich. “Energy Relaxation of Photoexcited Hot Electrons in GaAs.” In: *Phys. Rev. B* 8.12 (Dec. 15, 1973), pp. 5719–5727. doi: [10.1103/PhysRevB.8.5719](https://doi.org/10.1103/PhysRevB.8.5719). (Visited on 07/23/2025) (cited on page 45).
- [37] M. S. Skolnick et al. “Observation of a Many-Body Edge Singularity in Quantum-Well Luminescence Spectra.” In: *Phys. Rev. Lett.* 58.20 (May 18, 1987), pp. 2130–2133. doi: [10.1103/PhysRevLett.58.2130](https://doi.org/10.1103/PhysRevLett.58.2130). (Visited on 06/29/2022) (cited on page 45).
- [38] S. C. Jain et al. “Modified Simple Expression for Bandgap Narrowing in N-Type GaAs.” In: *Solid-State Electronics* 35.5 (May 1, 1992), pp. 639–642. doi: [10.1016/0038-1101\(92\)90030-G](https://doi.org/10.1016/0038-1101(92)90030-G). (Visited on 07/23/2025) (cited on page 45).

# Special Terms

## Numbers

**2DEG** two-dimensional electron gas. 34, 39, 45, 47

**2DHG** two-dimensional hole gas. 39

## C

**CCD** charge-coupled device. 40

## G

**GDQD** gate-defined quantum dot. 34

## O

**OAQD** optically active quantum dot. 34

## P

**PL** photoluminescence. 39, 41, 45–47, 49

**PLE** photoluminescence excitation. 47

**PSD** power spectral density. iii

## Q

**QCSE** quantum-confined Stark effect. 35–38

**QW** quantum well. 34–39, 43–46

## T

**TE** transverse electric. 41, 42

**TMM** transfer-matrix method. iv, 39, 41, 42

# Declaration of Authorship

I, Tobias Hangleiter, declare that this thesis and the work presented in it are my own and has been generated by me as the result of my own original research.

I do solemnly swear that:

1. This work was done wholly or mainly while in candidature for the doctoral degree at this faculty and university;
2. Where any part of this thesis has previously been submitted for a degree or any other qualification at this university or any other institution, this has been clearly stated;
3. Where I have consulted the published work of others or myself, this is always clearly attributed;
4. Where I have quoted from the work of others or myself, the source is always given. This thesis is entirely my own work, with the exception of such quotations;
5. I have acknowledged all major sources of assistance;
6. Where the thesis is based on work done by myself jointly with others, I have made clear exactly what was done by others and what I have contributed myself;
7. Parts of this work have been published before as:

- [1] Pascal Cerfontaine, Tobias Hangleiter, and Hendrik Bluhm. “Filter Functions for Quantum Processes under Correlated Noise.” In: *Phys. Rev. Lett.* 127.17 (Oct. 18, 2021), p. 170403. DOI: [10.1103/PhysRevLett.127.170403](https://doi.org/10.1103/PhysRevLett.127.170403).
- [2] Thomas Descamps, Feng Liu, Tobias Hangleiter, Sebastian Kindel, Beata E. Kardynał, and Hendrik Bluhm. “Millikelvin Confocal Microscope with Free-Space Access and High-Frequency Electrical Control.” In: *Rev. Sci. Instrum.* 95.8 (Aug. 9, 2024), p. 083706. DOI: [10.1063/5.0200889](https://doi.org/10.1063/5.0200889). (Visited on 08/12/2024).
- [3] Tobias Hangleiter, Pascal Cerfontaine, and Hendrik Bluhm. “Filter-Function Formalism and Software Package to Compute Quantum Processes of Gate Sequences for Classical Non-Markovian Noise.” In: *Phys. Rev. Research* 3.4 (Oct. 18, 2021), p. 043047. DOI: [10.1103/PhysRevResearch.3.043047](https://doi.org/10.1103/PhysRevResearch.3.043047). (Visited on 01/19/2022).
- [4] Tobias Hangleiter, Pascal Cerfontaine, and Hendrik Bluhm. “Erratum: Filter-function Formalism and Software Package to Compute Quantum Processes of Gate Sequences for Classical Non-Markovian Noise [Phys. Rev. Research 3, 043047 (2021)].” In: *Phys. Rev. Res.* 6.4 (Oct. 16, 2024), p. 049001. DOI: [10.1103/PhysRevResearch.6.049001](https://doi.org/10.1103/PhysRevResearch.6.049001). (Visited on 10/16/2024).

---

Aachen, July 28, 2025.